
Article:
Buckman, J, Mahoney, C orcid.org/0000-0002-2052-3576, März, C orcid.org/0000-0003-2558-4711 et al. (2 more authors) (2017) Identifying biogenic silica: Mudrock micro-fabric explored through charge contrast imaging. American Mineralogist, 102 (4). pp. 833-844. ISSN 0003-004X

https://doi.org/10.2138/am-2017-5797

Revision 2

Mudrock micro-fabric explored through charge contrast imaging

Buckman, Jim[a], Mahoney, Carol[b], März, Christian[c], Wagner, Thomas[d], & Blanco, Vladimir[e]

[a]*Institute of Petroleum Engineering, Heriot-Watt University, Riccarton, Edinburgh, EH14 4AS, Scotland.*

[b]*School of Civil Engineering and Geosciences, Cassie Building, Newcastle University, Newcastle upon Tyne, NE1 7RU, United Kingdom.*

[c]*School of Earth and Environment, University of Leeds, LS2 9JT, United Kingdom.*

[d]*The Lyell Centre, Heriot-Watt University, Riccarton, Edinburgh, EH14 4AS, Scotland.*

[e]*Instituto Colombiano del Petróleo, Ecopetrol, Bucaramanga, Colombia.*

Abstract: Visual inspection (optical microscope point counting) and silica abundance show that laminated shale from the Late Cretaceous of Colombia contains high levels of detrital quartz silt and sand particles. Closer examination using the charge contrast imaging (CCI) technique, however, illustrates that much of the quartz is authigenic micro-quartz, and thus not exclusively of detrital origin. In addition, many 'sand' grains that otherwise appear to represent simple detrital quartz particles are actually of biogenic origin, representing the tests of agglutinated foraminifera, formed from cemented silt-sized quartz particles. Finally, CCI shows that original detrital grains have undergone authigenic modification, with both syntaxial overgrowths and micro-quartz. Without recognition of these features, the relative proportion of detrital quartz (sand) would otherwise be greatly overestimated, with important implications for environmental interpretation. Furthermore, the recognition of biogenic structures, including agglutinated foraminifera, provides additional environmental information that otherwise could be easily overlooked.

Keywords: Shale, silt, quartz cementation

Introduction

Mudrocks represent approximately 65% of the stratigraphic record on continents (Ibbeken & Schleyer, 1991) and are a significant proportion of marine sediments (Blatt, 1970; Ibbeken & Schleyer, 1991). They are economically significant, representing sources and seals for hydrocarbon resources (Al-Bazali et al., 2005; Olabode et al., 2012) as well as potential seals for carbon dioxide storage / carbon sequestration (Olabode et al., 2012) and can contain metal enrichments up to low grade ore levels (Anjum et al., 2012). Although superficially simple and supposedly homogenous, mudrocks are highly variable at the micro-scale in terms of composition and texture (see examples in Camp et al., 2013; Milliken 2014; Milliken et al., 2016) documenting the complex overlying / integrated effects of dynamic primary depositional conditions and post-depositional diagenetic alteration. Comprising a wide range of dominantly clay-size clay minerals (smectite, illite, kaolinite), they also feature varying contents of silt and sand particles (quartz, feldspars and micas), organic matter (charcoal, kerogen, bitumen, phytoclasts), and siliceous and calcareous micro-skeletal materials (diatoms, radiolaria, foraminifera, etc). Fabric can range from massive to fissile (mudstone versus shale), and at the microscopic level, porosity / permeability, clay mineral composition and orientation can be drastically altered through diagenesis during burial, including the formation of authigenic phases such as calcite, quartz, pyrite, marcasite and iron-oxides. Mudrocks therefore provide a significant repository of information regarding the depositional environment and subsequent diagenetic changes through time, with their study becoming an increasing focus of research (Bennett et al., 1991; Camp et al., 2013; Lazar et al., 2015).

59 The present study illustrates detailed results from charge contrast imaging (CCI)
60 performed on a Cretaceous marine shale that has undergone substantial modification
61 through massive authigenic quartz induration. The content of quartz 'sand', defined as
62 quartz grains of 63 micrometer to 2 millimeter in diameter, in the shale had previously
63 been estimated based on Si content from XRF, XRD of the >2μm fraction and optical
64 microscope point counting of sand-sized grains in thin-section. Examination by scanning
65 electron microscopy (SEM) illustrates that much of the original depositional information
66 has been masked by pervasive silicification of the shale, a feature that is not obvious from
67 examination of hand specimens, thin-sections or element abundance patterns, therefore
68 leading to gross over-estimation of the original sand fraction.
69 We tested a low-vacuum SEM technique of charge contrast imaging (CCI) to elucidate
70 valuable information concerning the original depositional conditions of this shale. CCI
71 has previously been shown to have applications on a range of other geological materials,
72 where it has been utilized to illustrate crystal zoning, authigenic overgrowths, cement
73 fabrics and healed fractures (Watt et al., 2000; Doehne and Carson, 2001; Cuthbert and
74 Buckman, 2005; Buckman et al., 2016). The technique is comparable to
75 Cathodoluminescence within the SEM (Griffin 1997; Griffin 2000; Buckman et al.,
76 2016), with contrast being controlled by differences in surface conductivity through
77 subtle variations in composition and structural defects, affecting electron emission
78 (Buckman et al., 2016). As shown in this study, CCI provides highly valuable
79 information that improves the interpretation of silt bearing mudrocks which have
80 undergone heavy quartz cement precipitation (see Milliken, 2013; Milliken et al., 2016),
81 akin to applications on carbonate rocks (Buckman et al., 2016).

In addition, selected XRF and XRD data were collected to help interpretation of possible mechanisms for the observed occurrence of silicification.

Materials and Methods

The main sample examined (Z39) is a Late Cretaceous shale from the Coniacian of the Chipaque Formation from the Valle Medio del Magdalena (MMV) province, Colombia. The shale was collected from a surface outcrop at a road cutting in the Serranía de las Quinchas region (Fig. 1). An additional eight samples of 'shale' from the MMV and Eastern Cordillera (EC), from a range of stratigraphic horizons, related to Z39, and known burial depths, within the Cretaceous sequence (Fig. 2) were also examined and compared to the main sample. All samples were trimmed and impregnated with resin, then prepared as polished thin-sections, for examination by scanning electron microscopy (SEM). A Quanta 650 field-emission SEM was used, operated in low-vacuum mode, utilizing a large-field gaseous secondary electron detector (LF-GSED). Essentially, the charge contrast imaging (CCI) technique was used, following the method outlined in Buckman et al. (2016), which provides information similar to those achieved through cathodoluminescence (such as details of quartz overgrowths), by utilizing differences in surface charge build up, which effects image contrast and brightness. Thin-sections were examined uncoated, and images were collected at 20kV, with a spot size of 4.5, a detector bias of around 50% and a scan rate of between 5 and 20 µs. The standard quad backscattered electron (BSE) detector, and a Gatan mini-cathodoluminescence (CL) detector were utilized with similar imaging parameters to that of the LF-GSED, with the addition that for CL a scan rate of between 800 µs and 2.5 ms were used. In addition, an

105 Oxford Instruments X-Max^N 150 energy dispersive x-ray (EDX) detector was used for
106 elemental mapping, under the same operating conditions as for BSE imaging, with
107 between 20 and 30 full frame scans per map.
108 A Seimens model D500 XRD was used to analyse powdered samples, for both the greater
109 than 2 μm and the less than 2 μm fraction (35 samples). The less than 2 μm fraction were
110 analysed without treatment, with ethylene glycol (to differentiate expandable clays), and
111 thermally to differentiate kaolinite and chlorite. Samples were analysed from all
112 locations where thin-sections have been examined, with the exception of La Cristalina
113 and La Marina. Where possible, this included a sample from the same bed as the thin-
114 sections. Additionally, a single crushed whole rock sample of Z39 was analysed using a
115 Bruker D8 Advance powder diffractometer.
116 Samples from each location (184 samples) were also frozen, freeze-dried and ground in
117 an agate ball mill for subsequent chemical analysis by XRF (Philips PW 2400). Around
118 600 mg of each sample were mixed with 3600 mg of a 1 + 1 di-lithium tetraborate +
119 lithium metaborate ($Li_2B_4O_7$ + $LiBO_2$) mixture, pre-oxidized at 500˚C with NH_4NO_3, and
120 fused to homogeneous glass beads. Glass beads were analyzed for major and minor
121 elements. Analytical precision and accuracy were better than 5%, as checked by in-house
122 and international standard materials. Data were then used to calculate values for Zn/Al,
123 Cu/Al and Ni/Al, and an element enrichment factor (EEF) for Mo, V, U and Zn relative
124 to average shale (see Wedepohl, 1971).
125
126 **Results**

Analyses of backscattered (BSE) images of the thin-section (Z39) indicate that much of the shale is composed of quartz, with minor fine-sand particles, silt-size particles (typically up to 10 μm), a background of micro-quartz (sub-micrometer to micrometer-size), and illite clay (Fig. 3). In addition, high porosity is suggested, which is typically spherical to lenticular in morphology and excessively large (Fig. 3), indicating that much of this porosity is likely an artifact of grain plucking during sample preparation rather than a primary property of the shale**.**

Charge contrast images (CCI) taken using the LF-GSED confirm that the detrital grains are generally smaller than apparent from BSE imaging, having relatively thick syntaxial quartz overgrowths, and in many cases also incorporating authigenic micro-quartz (Fig. 4b-f). Some of the silt-size quartz particles display signs of healed cracks and fragmented grains that have been re-cemented (Fig. 4c). The micro-quartz that forms the bulk of the matrix has a distinctive mottled appearance when viewed by CCI, clearly differing from that of detrital quartz cores or associated syntaxial overgrowths (Figs. 4b-f, 5e). This authigenic micro-quartz is granular in appearance and typically around 1 μm or less in size (Fig. 5e). Subtle differentiation within the micro-quartz suggests multi-phased crystal growth with euhedral shaped overgrowths (Fig. 5e). In addition, some of the apparent larger 'silt' particles are in fact the compressed remains of agglutinated foraminifera (Fig. 5a-d). These remains are up to 100 μm in length, and typically around 40 μm in thickness, and vary in shape from lenticular to spherical or sub-spherical.

Unlike BSE or GSE images, CL-imaging proved of limited use with interpretation of the current material, producing low contrast images providing no additional information (Fig. 6). However, EDX mapping confirmed the pervasive nature of silicification (Fig. 6d).

150 Other thin-sections examined, from similar mudrocks within the Middle Magdelana
151 Valley (MMV) and adjacent Eastern Cordillera (EC), may also display a moderate to
152 high degree of silicification (sample LC224 and PE119), with the occurrence of both
153 large quartz overgrowths and common granular authigenic micro-quartz that are in the
154 order of a micrometer or less in size (Fig. 7a, b). Other samples, such as C29, have only
155 a low degree of silicification, with minor granular micro-quartz within the shale matrix
156 (Fig. 7c) and no obvious quartz overgrowths. The majority of other samples examined
157 exhibit limited silicification, with only isolated detrital quartz silt particles present (Fig.
158 7d-g). An exception to this is, however, sample A240, with localized areas of micro-
159 quartz that have a more wavy morphology rather than the previously noted granular
160 texture (Fig. 7h).
161 XRD results for the greater than 2 μm coarser fraction, shows highest values recorded for
162 clay and sand, with minimal values for other phases (Table 1). Particularly high levels of
163 'sand' are found from the Pescana and Zipa localities, including sample Z39. The high
164 occurrence of quartz 'sand' is also indicated by the additional whole rock analysis of Z39,
165 which is dominated by peaks for quartz, with minor illite (Fig. 8).
166 In general, XRD analysis of the less than 2 μm fraction, shows that illite-smectite is
167 almost solely limited to Crucero, illite is found throughout, with the highest values from
168 Quemado and Algodones, and some high records from Zipa (Table 1). Kaolinite is
169 common within Pescana, Crucero and Pedregal, but low within the other analysed areas,
170 while chlorite only occurs in very small levels within the Quemado and Algodones
171 material (Table 1). For micro-quartz, most areas are low with under 10%, with higher
172 values occurring from Pescana and Zipa (Table 1).

XRF results for the ratio of Zn/Al, Cu/Al and Ni/Al are presented for all sample locations (Table 2). These show relatively high enrichment in all three for sample Z39 and LC224, with some enrichment for Zn/Al in PE119 (including average values across each locality). The enrichment in Zn/Al is particularly notable for sample Z39 and even more so in LC224 (markedly so for the average value from La Cristalina). Results for the element enrichment factor (EEF) display marked enrichment in Mo, V, U and Zn for the Zipa and La Cristalina sections, and Mo is also relatively enriched in La Marina, Quemado and the Algodones localities (Table 3).

Discussion

The use of CCI to identify features within quartz, including silt-sized particles, has previously been documented (Milliken et al., 2007; Lehmann et al., 2009; Schieber, 2009). These CC images closely relate to images obtained through cathodoluminescence (Milliken et al., 2007; Lehmann et al., 2009; Milliken, 2013; Milliken et al., 2016), as is also the case for other geological materials (Watt et al., 2000; Buckman et al., 2016). CCI in comparison to SEM based CL, has the advantages of being faster and offering greater resolution (Buckman et al., 2016). Despite the use of high kV and long scan times, SEM-CL images (herein) of the silt particles, micro-quartz and siliceous biogenic structures do not shed much light on the internal structure of the grains, with the CL response being particularly weak (Fig. 6).

Both CL and CC imaging have been used for quartz to show evidence of *in situ* fracturing and re-cementation / healing (Watt et al., 2000), which also appears to be the case for some of the silt particles observed in the Colombian shale. The sparsity of such features

196 in our samples may be a consequence of the low number of genuine silt particles (<5%),
197 presenting limited opportunity for quartz grain-to-grain contact, as would be the case in
198 sandstone.
199 CC images of micro-quartz illustrate a mottled fabric for this sub-micrometer sized
200 material. To our knowledge, this is the first time that such a feature has been presented,
201 and confirms the variability of such material recently noted using CL in fine grained
202 shale (see Milliken et al., 2016, fig. 13b). The micro-quartz has a morphology that is
203 clearly distinct from both detrital quartz and associated syntaxial-quartz overgrowths.
204 Micro-quartz is differentiated by CCI, being typically granular in appearance (Fig. 3e, 4b,
205 5e), generally 1 μm or less in size, having a mottled appearance (Fig. 5e), and
206 occasionally with euhedral quartz overgrowths (Fig. 5e). Different from that, authigenic
207 syntaxial overgrowths on detrital quartz grains form simple euhedral forms (Fig 4b, e),
208 are often thick and occasionally exhibiting growth zonation. The latter can pass into rims
209 of amalgamated micro-quartz (Fig. 4b, e, f), which can greatly thicken the apparent size
210 of detrital grains. This distinction based on CCI is important as it provides a means of
211 differentiating detrital from authigenic quartz. Incorrect recognition of the micro-quartz
212 component could lead to overestimation of the detrital quartz (sand) input (see Table 1),
213 with important connotations for the interpretation of energy-levels during sedimentation
214 and consequently of the depositional environment (e.g., pelagic versus turbiditic and / or
215 contouritic deposition).
216
217 **Origins of silicification**

218 Quartz cements are a common feature of sedimentary basins with a range of sources,
219 including 1) metastable biogenic quartz, 2) dissolution of quartz grains by pressure
220 solution and 3) the release of silica through mineral reactions (Bjørlykke and Egeberg,
221 1993), such as through the smectite-illite transformation (Elliott and Matisoff, 1996;
222 Thyberg et al., 2010) and the alteration of volcanic glass and ash (Ghiara and Petti, 1995;
223 Rani et al., 2012). For the Colombian samples (Z39, LC224, which are most heavily
224 silicified), dissolution of quartz grains through pressure solution is unlikely to supply a
225 major component, as the low levels of silt or sand sized quartz particles provide very
226 limited opportunity for grain-to-grain contacts. However, presence of authigenic silica
227 from mineral interactions or from the remobilization of biogenic silica are both possible.
228 The degree of overburden and maximum recorded temperatures of the studied materials
229 (Table 4), combined with vitrinite reflectance values and a palaeothermal gradient of 20 –
230 25˚C (Parra et al., 2009), would be consistent with the transition of smectite to mixed
231 layer illite-smectite. Examination of an XRD trace for Z39, however, shows that there is
232 no evidence of smectite or mixed layer smectite-illite (Fig. 8), or from the Zipa section
233 (Table 1), although the very presence of illite indicates that the transformation cannot be
234 totally excluded. If clay transformation was responsible for the release of silica, it would
235 have occurred after relatively high levels of compaction (see Table 4 for degree of
236 overburden), which is inconsistent with the presence of abundant 'granular' micrometer
237 sized micro-quartz. Furthermore, if clay transformation were to explain the occurrence of
238 micro-quartz within the Chipaque Formation, then the degree of silicification might be
239 expected to increase with depth (with higher temperature), which is not the case for the
240 current associations (Table 4, Fig. 7). We recognize, however, that some minor

241 silicification deeper within the sequence from the Eastern Cordillera may have an origin
242 from clay mineral transition, leading to a more irregular and often compressed
243 morphology (Fig. 7h), although the degree of silicification is here lower (Table 4). The
244 latter would certainly have passed through the temperature window necessary for the
245 transformation of smectite to illite, with associated release of silica, as indicated by the
246 occurrence of chlorite (Table 1), which within shales can form at temperatures of over
247 122˚C (Hurst, 1985). Volcanic activity, producing thin ash deposits, has been noted from
248 the La Luna Formation, Magdelana Valley (Galvis-Portilla et al., 2014). The latter is
249 stratigraphically equivalent to the Chipaque Formation (Guerrero, 2002), with in excess
250 of 78 ash beds recorded in a 3 to 4 metre section at the Cenomanian-Turonian boundary
251 (Erlich et al., 2003). Also, bentonite beds are present at the Cenomanian-Turonian
252 boundary within the Chipaque Formation within the Eastern Cordillera (Villamil and
253 Arango, 1994). However, Vergara (1997) has indicated that volcanic activity where
254 present in Colombia, although likely to increase marine productivity, was unlikely to be a
255 direct source of silicification. Dissolution of volcanic ash deposits and glass are unlikely
256 to contribute significantly to the observed micro-quartz production, as no direct evidence
257 of volcanic deposits have been recorded interbedded within the current heavily silicified
258 locations (Zipa and La Cristalina).
259 Another potential source of silica for the formation of micro-quartz could have been
260 metastable biogenic opal, from sponge spicules, diatom frustules or radiolaria. While no
261 direct physical evidence of biogenic opal was observed in our study samples, pyritized
262 sponge spicules have been noted from other horizons within the basin (from Pescana
263 within P145 and La Cristalina in LC224, Fig. 9), supporting a release mechanism from

264 biogenic silica. Geochemical support for the original deposition of biogenic opal comes
265 from a significant enrichment of trace elements (Cu, Ni, and Zn, see Table 2), all of
266 which are typical for upwelling settings, such as modern Namibia and Peru (Brumsack,
267 2006). In such upwelling settings, high primary productivity mainly by diatoms leads to
268 elevated export of large amounts of biogenic opal and organic matter enriched in trace
269 metals to the seafloor, where they get partly buried under typically reducing conditions.
270 Enrichment in Zn, Cu and Ni from the Chipaque Formation (at Zipa, including Z39), and
271 underlying Fomeque Formation (at La Cristalina, including LC224) from the MMV
272 (Table 2), and of Zn within the Chipaque Formation (at Pescana, including PE119) from
273 the EC (Table 2), strongly suggests that silicification within these horizons (with high to
274 moderate silicification) was primarily due to dissolution and migration of biogenic silica,
275 originally produced through high marine productivity. This conclusion is further
276 supported by the occurrence of a thick fractured chert horizon (from the Lidita
277 Formation) that directly overlies the Chipaque Formation (Garcia-Gonzalez, 2010). This
278 has been interpreted as representing regional high productivity linked to vigorous
279 upwelling (Villamil et al., 1999). Chert formation has been frequently documented from
280 the Cenomanian to Santonian across the northern part of South America, including the
281 EC and MMV (Tribovillard et al., 1991 ; Perez-Infante, 1996; Arango and Hay, 1999),
282 often linked with upwelling processes (Macellari and DeVries, 1987). Palaeogeographic
283 reconstructions for the wider area (Fig. 10) support regional upwelling, driven by
284 prevailing trade winds from the north-east (Erlich et al., 2003), further supporting an
285 origin for silicification from remobilization of biogenic silica.
286

Significance of benthic foraminifera

Agglutinated foraminifera tests, composed of detrital quartz and feldspar particles, have recently been illustrated for 'cherty stringers' in Carboniferous and Devonian black shales (Milliken et al., 2007; Schieber, 2009). Such foraminifera have also been previously recorded from Cretaceous deep-sea black shales (e.g. Mello, 1971), including benthic agglutinated and pelagic foraminifera from the Chipaque Formation (Vergara et al., 1997). The recognition, through CCI, of agglutinated foraminifera, shallow infaunal foragers and suspension feeders that strictly require oxygen (Kaminski & Schroder, 1987), implies that bottom waters or near-surface sediments were at least episodically dysaerobic during deposition, if not fully aerobic. Repetitive alternations between fully aerobic and slightly oxygen-depleted conditions are indeed suggested from the general lack of pyrite and other sulphide phases (Table 1). This SEM-based redox interpretation clearly contrasts with the overall enrichment of redox-sensitive / sulphide-forming trace elements (Mo, V, U, Zn) measured in the same sample, a pattern which is commonly related to anoxic or even sulfidic bottom and pore water conditions (Brumsack, 2006). Such discrepancies between geochemistry- and micropaleontology-based redox interpretations are not unusual and may actually be expected. It has been shown that some benthic agglutinated foraminifera are anoxia-tolerant through the process of intracellular denitrification (Schieber, 2011). Milliken et al., (2007) also note that modern agglutinated foraminifera are highly tolerant to conditions of low oxygenation. Furthermore, benthic foraminifera can colonize previously anoxic seafloor during short-termed re-oxygenation events rather quickly whereas element geochemistry will still record dominantly anoxic conditions, leading to the well known "anoxic benthic

310 foraminifera" paradox (Friedrich, 2010). We therefore propose that aerobic near-surface
311 sediment and bottom water conditions prevailed, but were temporally and spatially
312 restricted.
313 Assuming that the agglutinated foraminifera are *in situ*, rather than resuspended via
314 bottom currents, their occurrence suggests that the surface sediments were soft and that
315 strong surface water flow or scouring was absent (Kaminski & Schroder, 1987). This
316 would argue for a pelagic rather than turbidite or contourite depositional setting. To
317 emphasize, such an interpretation may well have been inferred from the apparent copious
318 occurrence of silt and sand particles. Given that it has been shown that different
319 agglutinated foraminifera morphotypes are found associated with a particular water
320 depth, infaunal niche, and oxygen levels (Kaminski et al*.,* 1995), further studies may well
321 prove interesting, but are beyond the scope of this manuscript.
322 The spherical to lenticular porosity, which is a common feature of the Colombian shale
323 (Z39), has a number of possible interpretations. In the case of the lenticular shaped
324 pores, these likely represent the locations of agglutinated benthic foraminifera that have
325 been plucked from the shale during sample preparation. More spherical pores may
326 instead represent sections through other agglutinated foraminifera, such as illustrated
327 herein (Fig. 5c, d), that have suffered a similar fate. They may alternatively represent
328 calcareous pelagic foraminifera (see Vergara et al, 1997), where the test has suffered
329 dissolution during diagenesis, or silicified algal cells (*Tazmanites*), such as those
330 illustrated from Devonian black shales by Schieber (1996), which have also been lost
331 during sample preparation. A number of these pores show an association between carbon
332 and sulphur, so may represent the remnants of *Tazmanites* (silicified or otherwise) or

possibly ‘organic’ filled remnants of dissolved pelagic foraminifera. *Tazmanites* has been clearly observed in other Colombian black shales (*pers. obs*.). If, as seems likely, a proportion of the pores represent plucked-out benthic agglutinated foraminifera, this would be of particular interest, as it supports the widespread distribution of such foraminifera, and thus rapid fluctuations in seafloor oxygenation levels through time.

Implications

Charge contrast imaging (CCI) enables differentiation of detrital and authigenic quartz components within the silt-size fraction of mudrocks, comparable to applications on carbonates and arenites. In particular, the characteristic mottled appearance of authigenic micro-quartz clearly separates it from detrital silt-sized particles of quartz. Without complementary data from CCI, the quartz sand component of a shale can easily be overestimated if only apparent detrital grain size and elevated relative Si contents are considered. This has profound implications for the interpretation of hydrodynamics of the environment of deposition; possibly representing lower-energy conditions than would otherwise have been interpreted from apparent high-levels of quartz silt. We show that CCI unambiguously identifies the presence of agglutinated foraminifera, which provide additional information on the depositional environment that might otherwise be overlooked, such as degree of sediment / water interface oxygenation levels, sediment consistency, and hydrodynamics. In addition, CCI provides information of a similar character to that usually supplied by CL, although with an improvement in resolution and speed of acquisition. The high levels of silicification recorded from the Zipa and La Cristalina sections represent relatively early micro-quartz formation, with silica sourced

356 from siliceous micro-organisms, forming pervasive micrometer sized granular masses.
357 This contrasts with wavy micro-quartz noted from the Algodones area, formed from the
358 smectite-illite transformation at greater depth within the basin.
359

360 **Acknowledgements**

361 Nelson Sanchez and Freddy Niño from Ecopetrol for providing study samples, data and
362 geological background information. Ecopetrol provided funding for the analysis and the
363 project. Bernhard Schnetger (ICBM, Oldenburg) for XRF analysis. Georgina Rosair
364 provided XRD analysis (Fig. 8). This manuscript has also been improved through the
365 comments of Kitty Milliken, Mathias Bernet and Lynda Williams, which we greatly
366 appreciate.
367

References

Al-Bazali, T.M., Zhang, J., Chenevert, M.E., and Sharma, M.M. (2005) Measurement of the sealing capacity of shale caprocks. SPE Annual Technical Conference and Exhibition, Dallas, Texas, USA, 9-12 October 2005.

Anjum, F., Shahid, M., and Akcil, A. (2012) Biohydrometallurgy techniques of low grade ores: a review on black shales. Hydrometallurgy, 117-118, 1-12

Arango, C., and Hay, W.W. (1999) Plate tectonic paleoceanographic hypothesis for Cretaceous source rocks and cherts of northern South America. Evolution of the Cretaceous ocean-climate, 191.

Bennett, R.H., Bryant, W.R., and Hulbert, M.H. (1991) Microstructure of Fine-grained Sediments, from Mud to Shale, 582 p. Springer-Verlag, New York.

Bjørlykke, K., and Egeberg, P.K. (1993) Quartz cementation in sedimentary basins. AAPG Bulletin, 77, 1538-1548.

Buckman, J.O., Corbett, P.W.M., and Mitchell, L. (2016) Charge contrast imaging (CCI): revealing enhanced diagenetic features of a coquina limestone. Journal of Sedimentary Research, 86, 734-748.

Blatt, H. (1970) Determination of mean sediment thickness in the crust: a sedimentologic method. Geological Society of America Bulletin, 81, 255-262.

Brumsack, H.J. (2006) The trace metal content of recent organic carbon-rich sediments: implications for Cretaceous black shale formation. Palaeogeography, Palaeoclimatology, Palaeoecology, 232, 344–361

389 Camp, W.K., Diaz, E., and Wawak, B. (2013) Electron microscopy of shale
390 hydrocarbon reservoirs, memoir 102. The American Association of Petroleum
391 Geologists, Tulsa, 260 p.
392 Cuthbert, S.J., and Buckman, J.O. (2005) Charge contrast imaging of fine-scale
393 microstructure and compositional variation in garnet using the environmental scanning
394 electron microscope. American Mineralogist, 90, 701-707.
395 Doehne, E., and Carson, D. (2001) Charge contrast imaging (CCI) in the environmental
396 scanning electron microscope: optimizing operating parametres for calcite. Microscopy
397 and Microanalysis, 7, 780-781.
398 Elliott, W.C., and Matisoff, G. (1996) Evaluation of kinetic models for the smectite to
399 illite transformation. Clays and Clay Minerals, 44, 77-87.
400 Erlich, R.N., Villamil, T., and Keens-Dumas, J. (2003) Controls on the deposition of
401 Upper Cretaceous organic carbon-rich rocks from Costa Rica to Suriname. In C.
402 Bartolini, R.T. Buffler, and J. Blickwede, eds., The Circum-Gulf of Mexico and the
403 Caribbean: Hydrocarbon habitats, basin formation, and plate tectonics: AAPG Memoir
404 79, 1-45.
405 Friedrich, O. (2010) Benthic foraminifera and their role to decipher paleoenvironment
406 during mid-Cretaceous Oceanic Anoxic Events – the “anoxic benthic foraminifera”
407 paradox. Revue de Micropaleontologie, 53, 175-192.
408 Galvis-Portilla, H.A., Higuera-Diaz, I., Cespedes, S., Ballesteros, C., Forero, S., Marfisi,
409 N., Cantisano, M, Pineda, E., Pachon, Z., Slatt, R.M., Ramirez, R., Guzman, G., and
410 Torres, A. (2014) Regional sequence stratigraphy of the Upper Cretaceous La Luna

411 Formation in the Magdalena Valley Basin, Colombia. Unconventional Resources
412 Technology Conference, Denver, Colorado, USA, 25-27 August 2014.

413 Garcia-Gonzalez, M. (2010) Shale gas potential in the Eastern Cordillera of
414 Colombia. AAPG Bulletin, 10286.

415 Ghiara, M.R., and Petti, C. (1995) Chemical alteration of volcanic glasses and related
416 control by secondary minerals: Experimental studies. Aquatic Geochemistry, 1, 329-354.

417 Gómez Tapias, J., and Almanza Meléndez, M.F. (ed) (2015) Compilando la Geología de
418 Colombia: Una visión a 2015. Servicio, Geológico Colombiano, Publicaciones
419 Geológicas Especiales 33.

420 Griffin, B.J. (1997) A new mechanism for the imaging of crystal structure in non-
421 conductive materials: an application of charge-induced contrast in the environmental
422 scanning electron microscope (ESEM). Microscopy and Microanalysis, 3, 1197-1198.

423 Griffin, B.J. (2000) Charge contrast imaging of material growth and defects in ESEM:
424 linking electron emission and cathodoluminescence. Scanning, 22, 234.

425 Guerrero, J. (2002) A proposal on the classification of systems tracts: Application to the
426 allostratigraphy and sequence stratigraphy of the Cretaceous Colombian Basin. Part 2:
427 Barremian to Maastrichtian. Geología Colombiana, 27, 27-49.

428 Hurst, A. (1985) Diagenetic chlorite formation in some Mesozoic shales from the
429 Sleipner area of the North Sea. Clay Minerals, 20, 69-79.

430 Ibbeken, H., and Schleyer, R. (1991) Source and Sediment: A Case Study of Provenance
431 and Mass Balance at an Active Plate Margin (Calabria, Southern Italy), 286 pp. Springer-
432 Verlag, New York.

433 Kaminski, M.A., and Schroder, C.J. (1987) Environmental analysis of deep-sea
434 agglutinated foraminifera: can we distinguish tranquil from disturbed environments?
435 Gulf Coast Section SEPM Foundation Proceedings of the 8th Annual Research
436 Conference, 90-93.

437 Kaminski, M.A., Boersma, A., Tyszka, J., and Holbourn, A.E.L. (1995) Response of
438 deep-water agglutinated foraminifera to dysoxic conditions in the California Borderlands
439 basins. In Kaminski, M.A., Geroch, S., and Gasinski, M.A. (eds), Proceedings of the
440 Fourth International Worksop on Agglutinated Foraminifera, Kraków Poland, September
441 12-19, 1993, pp. 131-140. Grzybowski Foundation Special Publication no 3.

442 Lazar, O.R., Bohacs, K.M., Macquaker, J.H.S., Schieber, J., and Demko, T.M. (2015)
443 Capturing key attributes of fine-grained sedimentary rocks in outcrops, cores, and thin
444 sections: nomenclature and description guidelines. Journal of Sedimentary Research, 85,
445 230-246.

446 Lehmann, K., Berger, A., Götte, T., and Wiedenbeck, M. (2009) Growth related
447 zonations in authigenic and hydrothermal quartz characterized by SIMS, EPMA, SEM-
448 CL- and SEM – CC-imaging. Mineralogical Magazine, 73, 633-643.

449 Macellari, C.E., and DeVries, T.J. (1987) Late Cretaceous upwelling and anoxic
450 sedimentation in northwestern South America. Palaeogeography, Palaeoclimatology,
451 Palaeoecology, 59, 279-292.

452 Mello, J.F. (1971) Foraminifera from the Pierre Shale (Upper Cretaceous) at Red Bird,
453 Wyoming. Geological Survey Professional Paper 393-C, United States Government
454 Printing Office, Washington, 53 p., 7 plates.

455 Milliken, K.L., Choh, S.-J., Papazis, P., and Schieber, J. (2007) "Cherty" stringers in the
456 Barnett Shale are agglutinated foraminifera. Sedimentary Geology, 198, 221-232.

457 Milliken, K.L. (2013) SEM-based cathodoluminescence imaging for discriminating
458 quartz types in mudrocks. Unconventional Resources Technology Conference, Denver,
459 Colorado, USA. URTeC 1582467.

460 Milliken, K. (2014) A compositional classification for grain assemblages in fine-grained
461 sediments and sedimentary rocks. Journal of Sedimentary Research, 84, 1185-1199.

462 Milliken, K.L., Ergene, S.M., and Ozkan, A. (2016) Quartz types, authigenic and
463 detrital, in the Upper Cretaceous Eagle Ford Formation, South Texas, USA. Sedimentary
464 Geology, 339, 273-288.

465 Mora, A., Casallas, W., Ketcham, R.A., Gomez, D., Parra, M., Namson, J., and Ghorbal,
466 B. (2015) Kinematic restoration of contractional basement structures using
467 thermokinematic models: a key tool for petroleum system modelling. AAPG Bulletin,
468 99, 1575-1598.

469 Olabode, A., Bentley, L., and Radonjic, M. (2012) Shale caprock integrity under carbon
470 sequestration conditions. Porous Media and its Applications in Science, Engineering, and
471 Industry. American Institute of Physics Conference Proceedings, 1453, 347-352.

472 Parra, M., Mora, A., Sobel, E.R., Strecker, M.R., and González, R. (2009) Episodic
473 orogenic front migration in the northern Andes: Constraints from low-temperature
474 thermochronology in the Eastern Cordillera, Colombia. Tectonics, 28, TC4004,
475 doi:10.1029/2008TC002423.
476 Perez-Infante, J., Farrimond, P., and Furrer, M. (1996) Global and local controls
477 influencing the deposition of the La Luna Formation (Cenomanian – Campanian),
478 western Venezuela. Chemical Geology, 130, 271-288.

479 Rani, N., Shrivastava, J.P., Bajpai, RKJ. (2012) Near hydrothermal alteration of
480 obsidian glass: Implications for long term performance assessments. Journal of the
481 Geological Society of India, 79, 376-382.

482 Schieber, J. (1996) Early diagenetic silica deposition in algal cysts and spores: a source of
483 sand in black shales? Journal of Sedimentary Research, 66, 175-183.

484 Schieber, J. (2009) Discovery of agglutinated benthic foraminifera in Devonian black
485 shales and their relevance for the redox state of ancient seas. Paleogeography,
486 Paleoclimatology, Paleoecology, 271, 292-300.
487 Schieber, J. (2011) Styles of agglutination in benthic foraminifera from modern Santa
488 Barbara Basin sediments and the implications of finding fossil analogs in Devonian and
489 Mississippian black shales, p 573-590. In Altenbach, A.V., Bernard, J.M., and Seckbach,

490 J. (eds.), Anoxia: evidence of eukaryote survival and paleontological strategies. Springer
491 Science and business media, 648 p.
492 Thyberg, B., Jahren, J., Winje, T., Bjørlykke, K., Faleide, J.I., and Marcussen, Ø. (2010)
493 Quartz cementation in Late Cretaceous mudstones, northern North Sea: Changes in rock
494 properties due to dissolution of smectite and precipitation of micro-quartz crystals.
495 Marine and Petroleum Geology, 27, 1752-1764.
496 Tribovillard, N.P., Stephan, J.F., Manivit, H., Reyre, Y., Cotillon, P., and Jautée, E.
497 (1991) Cretaceous black shales of Venezuelan Andes: preliminary results on stratigraphy
498 and paleoenvironmental interpretations. Palaeogeography, Palaeoclimatology,
499 Palaeoecology, 81, 313-321.
500 Vergara, L.S. (1997) Stratigraphy, foraminiferal assemblages and paleoenvironments in
501 the Late Cretaceous of the Upper Magdalena Valley, Colombia (Part I). Journal of South
502 American Earth Sciences, 10, 111-132.
503 Vergara, L., Rodríguez, G., and Martínez, I. (1997) Agglutinated foraminifera and
504 sequence stratigraphy from the Chipaque Formation (Upper Cretaceous) of El Crucero
505 Section, Colombia, South America. Micropaleontology, 43, 185-201.
506 Villamil, T., & Arango, C. (1994) High-resolution analyses of the Cenomanian-Turonian
507 Boundary in Colombia: evidence for sea level rise, condensation and upwelling.
508 Mesozoic-Cenozoic stratigraphy and tectonic evolution of the Caribbean Region /
509 Northern South America: Implications for eustasy from exposed sections of a Cretaceous-
510 Eocene passive margin setting. - SEPM special publication
511 Villamil, T., Arango, C., and Hay, W.W. (1999) Plate tectonic paleoceanographic
512 hypothesis for Cretaceous source rocks and cherts of northern South America. In Barrera,

513 E., and Johnson, C.C. (eds), Evolution of the Cretaceous Ocean-Climate system, 191-202.
514 Geological Society of America, Special Paper 332.
515 Watt, G.R., Griffin, B.J., and Kinny, P.D. (2000) Charge contrast imaging of geological
516 materials in the environmental scanning electron microscope. American Mineralogist,
517 85, 1784-1794.
518 Wedepohl, K.H. (1971) Environmental influences on the chemical composition of
519 shales and clays. Physics and Chemistry of the Earth, 8, 305-333.
520
521

522 **Figure Captions**

523

524 **Figure 1.** **a**) Locality map, showing geological units, and locality of sample Z39 from
525 the Chipaque Formation. Locations of other samples illustrated in the current work also
526 given. Both location names and sample identifiers are given. **b**) General location map,
527 with context of area in (**a**) shown in white box. MMV = Middle Magdelana Valley, EC =
528 Eastern Cordillera. After Gómez Tapias and Almanza Meléndez (2015).

529

530 **Figure 2.** Stratigraphic distribution of formations and major facies within the Middle
531 Magdelana Valley (MMV) Basin and Eastern Cordillera (EC). Approximate
532 geographical and stratigraphic position of all samples marked: (1) Z39, (2) LC224, (3)
533 PE119, (4) C29, (5) P145, (6) M320, (7) P1+100, (8) Q1+70, (9) A240. Generalised
534 stratigraphy based on Parra et al., (2009). C= Conaician, T= Turonian.

535

536 **Figure 3.** **a**) Backscattered (BSE) stitched image of the whole polished thin-section for
537 sample Z39, showing lamination. **b**) BSE image of area marked in (**a**), displaying detail
538 of lamination, lenticular (*L*) and spherical (*S*) porosity, and pore lining Fe oxides (*Fe*).
539 Large porosity may be an artifact of plucking during sample preparation. **c**) BSE image
540 of detrital quartz silt particles (*Dq*) and authigenic micro-quartz (*Mq*). **d**) and **e**) BSE
541 and charge contrast matched pair of micrographs, illustrating micro-quartz (*Mq*) in
542 association with clay (*Cy*). All images are of sample Z39.

543

Figure 4. SEM micrographs illustrating fabric of silicified shale (Z39). **a**) Backscattered electron image (BSE), **b**) – **f**) gaseous secondary electron images (GSE), exhibiting charge contrast (CC), illustrating a number of features. In (**a**), a large silt particle (*St*) is surrounded by authigenic micro-quartz (*Mq*). Silt particle appears to be 15 μm long. In (**b**), charge contrast imaging (CCI) demonstrates that the detrital quartz (*Dq*) silt grain also comprises an authigenic 'syntaxial' quartz overgrowth (*Qo*), as well as authigenic micro-quartz (*Mq*). Similar relationships are also shown in (**c**) to (**f**). In addition in (**c**), healed fractures (*f*) are observed, testifying to periods of compaction and grain shattering prior to cementation. Note polishing scratches (s) on slides may be highlighted by the CCI technique.

Figure 5. Charge contrast SEM micrographs illustrating occurrence of siliceous biogenic structures and nature of micro-quartz cement within sample Z39. **a**) – **b**) Agglutinated foraminifera, longitudinal section, overview and expanded view. Key as in figure 4, with addition of agglutinated foraminifera (*Af*). Note lenticular shape in **a**) and the individual quartz silt particles in (**b**). **c**) – **d**) Agglutinated foraminifera, transverse section, overview and expanded view. Note the occurrence of clay (*Cy*), and individual silt particles with syntaxial overgrowths (*1-6*). **e**) Detail of mottled micro-quartz, each around 1 μm or less in size. Note euhedral shape to some of the micro-quartz (*Eo*).

Figure 6. Comparison of **a**) backscattered, **b**) charge contrast image, **c**) cathodoluminescence image, and **d**) energy dispersive x-ray (EDX) map; all images taken of the same field of view from sample Z39. (**b**) Shows the boundary between detrital

core and overgrowth (arrows). Cathodoluminescence image in (**c**) displays poor contrast and lack of detail, which is atypical of CL, despite the use of high kV (20kV), large spot size and long dwell times. X-ray dot map in (**d**) indicates quartz (1), clays (2), and pores (3).

Figure 7. Charge contrast SEM micrographs illustrating degree of authigenic siliceous micro-quartz cement, through the stratigraphic succession, in comparison to Z39: **a**) LC224 (La Cristalina), **b**) PE119 (Pescana), **c**) C29 (Crucero), **d**) P145 (Pedregal), **e**) M364 (La Marina), **f**) P1+100 (Pedregal), **g**) Q1+70 (Quemado), **h**) A240 (Algodones). **a**) – **h**) Increasing in stratigraphic depth (see Table 4). **a**), **b**) High silicification, with plentiful quartz overgrowths on detrital quartz silt grains, and micro-quartz, **c**) low degree of silicification, comprising small amount of authigenic micro-quartz, **d**) - **g**) no to limited occurrence of micro-quartz (only small quartz silt particles), **h**) low degree of silicification, with localized areas displaying micro-quartz with a wavy morphology. Note **a**) from Middle Magdelana Valley (MMV) and **b**)-**h**) from Eastern Cordillera (EC).

Figure 8. XRD trace for sample Z39, showing prevalence of quartz (all unlabeled peaks), with minor illite (indicated by d-spacing values). Note the lack of peaks associated with smectite that would appear on the far left-hand side of the graph. Two minor peaks occur on the left-hand side (denoted by ?), but have no clear identity. Sample analysed through powder XRD using Cu target, of the whole sample, with no treatment other than crushing to a fine powder. Analysis of Z39 (<2um fraction) with glycolation confirms lack of illite-smectite, the presence of minor kaolinite and dominance of illite (Table 1).

590

591 **Figure 9.** BSE SEM micrograph, illustrating the dissolution of biogenic silica (from a
592 sponge spicule) and replacement with pyrite, from the Fomeque Formation (sample
593 LC224, La Cristalina).

594

595 **Figure 10.** Palaeogeographical reconstruction, during the Upper Cretaceous, within the
596 study area. Based on Arango and Hay (1999). Illustrating the general distribution of
597 facies, and orientation of the depositional basin. Basin connected to open ocean to the
598 north-east. Areas illustrated that are rich in chert and or phosphatic–rich deposits indicate
599 high productivity rates. Small black arrows indicate location of "wind-driven" upwelling,
600 white arrows direction of shallow water flow, grey arrows river flow, and large black
601 arrow direction of trade winds, after Erlich et al., (2003) and Arango and Hay (1999).

602

603

Table Captions

Table 1. XRD data for the greater than 2 μm and less than 2 μm fractions from locations within the current study. Samples from beds examined in thin-section during the study are in ***bold italic***. Data gathered using a Siemens D500 XRD. Key: Carb = carbonate, I/S = illite-smectite, I = illite, K = kaolinite, ND = none detected, TR = trace levels. Note no data collected from La Cristalina (e.g. LC224) or La Marina (e.g. M364), which is indicated by X. Locations arranged in approximate stratigraphic order.

Table 2. XRF data for Zn/Al, Cu/Al and Ni/Al. Sample # refers to the examined thin-sections, while data within brackets is an average figure for the different recorded locations. Number of samples is 18, 20, 50, 25, 17, 21, 17, 12 and 21 respectively. Samples arranged in approximate stratigraphic order.

Table 3. Element enrichment factors (EEF) for Mo, V, U and Zn relative to average shale (Wedepohl, 1971). Areas that are relatively enriched are shaded in light grey.

Table 4. Table of data for samples examined during the current study. With data on location, formation, stage, description, degree of silicification, overburden, and temperature. Overburden and temperature data from Mora et al., (2015). Note figures in brackets for temperature refer to the degree of error. Samples arranged in approximate stratigraphic order. MMV = Middle Magdelana Valley, EC = Eastern Cordillera, * with kaolinite and detrital quartz filled burrows, ** irregular wavy authigenic micro-quartz with clay.

Table 1

Location	>2 µm						<2 µm				
	Clay	Sand	Feldspar	Carb	Pyrite	TiO_2	I/S	I	K	Micro-quartz	Chlorite
PESCANA	***23***	***60***	***7***	***ND***	***<5***	***TR***	***ND***	***27***	***59***	***14***	***ND***
	68	17	<5	ND	ND	<5	13	28	54	5	ND
	38	52	<5	ND	TR	TR	ND	63	32	5	ND
	10	85	TR	ND	TR	TR	ND	34	34	32	ND
	27	68	ND	ND	ND	TR	ND	23	58	19	ND
	8	77	<5	TR	<5	TR	ND	18	18	64	ND
ZIPA	14	81	TR	ND	ND	TR	ND	60	<5	35	ND
	<5	90	ND	ND	ND	ND	ND	42	<5	53	ND
	39	56	ND	ND	TR	TR	ND	90	5	5	ND
	10	***85***	***ND***	***ND***	***ND***	***TR***	***ND***	***82***	***<5***	***13***	***ND***
	25	70	ND	ND	TR	TR	ND	68	12	20	ND
	11	84	ND	ND	TR	TR	ND	73	<5	22	ND
LA CRISTALINA	X	X	X	X	X	X	X	X	X	X	X
CRUCERO	62	33	TR	ND	ND	TR	15	20	45	20	ND
	63	***27***	***TR***	***ND***	***TR***	***<5***	***22***	***13***	***59***	***6***	***ND***
	77	18	TR	ND	TR	TR	18	23	50	9	ND
	35	55	ND	ND	TR	<5	25	50	20	<5	ND
	77	18	TR	ND	TR	TR	43	25	32	ND	ND
	74	21	TR	ND	TR	TR	8	47	40	<5	ND
PEDREGAL	65	20	TR	ND	<5	<5	ND	63	37	ND	ND
	38	42	<5	ND	5	<5	5	65	25	<5	ND
	46	39	TR	<5	TR	<5	ND	45	49	6	ND
	25	65	ND	ND	ND	<5	ND	50	40	10	ND
	63	22	TR	ND	<5	<5	ND	65	35	ND	ND
	38	47	TR	ND	<5	<5	ND	66	34	ND	ND
LA MARINA	X	X	X	X	X	X	X	X	X	X	X
QUEMADO	46	44	TR	ND	5	ND	ND	82	4.5	5	8
	50	40	<5	ND	TR	ND	ND	94	ND	6	ND
	60	25	<5	ND	<5	ND	ND	70	9	9	12
	52	33	<5	ND	<5	ND	ND	80	<5	10	<5
	38	52	<5	ND	ND	ND	ND	100	ND	ND	ND
ALGODONES	57	33	<5	ND	ND	ND	ND	95	ND	<5	ND
	50	40	<5	ND	TR	ND	ND	95	ND	<5	ND
	65	***20***	***<5***	***ND***	***<5***	***ND***	***ND***	***90***	***<5***	***<5***	***ND***
	86	9	TR	ND	ND	ND	ND	59	25	ND	16
	55	40	TR	ND	ND	ND	ND	76	15	ND	9
	67	23	<5	ND	ND	ND	ND	95	ND	<5	ND

Table 1. XRD data for the greater than 2 µm and less than 2 µm fractions from locations within the current study. Samples from beds examined in thin-section during the study are in ***bold italic***. Data gathered using a Siemens D500 XRD. Key: Carb = carbonate, I/S = illite-smectite, I = illite, K = kaolinite, ND = none detected, TR = trace levels. Note no data collected from La Cristalina (e.g. LC224) or La Marina (e.g. M364), which is indicated by X. Locations arranged in approximate stratigraphic order.

Table 2

Sample #	Location	Zn/Al	Cu/Al	Ni/Al
PE119	Pescana	6.94 (10.85)	0.71 (0.41)	1.65 (2.18)
Z39	Zipa	27.25 (66.65)	8.81 (7.32)	9.02 (16.88)
LC224	La Cristalina	67.53 (254.92)	4.49 (11.75)	22.27 (37.86)
C29	Crucero	1.69 (4.97)	0.52 (0.44)	1.03 (1.57)
P145	Pedregal	2.75 (4.93)	1.01 (1.17)	3.21 (2.87)
M364	La Marina	4.51 (5.59)	0.36 (0.51)	0.93 (1.99)
P1+100	Pedregal	1.48 (4.93)	0.74 (1.17)	1.27 (2.87)
Q1+70	Quemado	1.42 (1.95)	2.84 (1.6)	4.15 (2.89)
A240	Algodones	4.18 (4.38)	1.58 (1.61)	3.07 (2.52)

Table 2. XRF data for Zn/Al, Cu/Al and Ni/Al. Sample # refers to the examined thin-sections, while data within brackets is an average figure for the different recorded locations. Number of samples is 18, 20, 50, 25, 17, 21, 17, 12 and 21 respectively. Samples arranged in approximate stratigraphic order.

Table 3.

Location	Mo EEF	V EEF	U EEF	Zn EEF
Pescana	0.77	0.79	1.86	0.99
Zipa	11.63	7.32	8.59	6.06
La Cristalina	139.90	29.66	9.73	23.17
Crucero	1.28	0.71	1.44	0.45
Pedregal	0.23	0.68	2.24	0.45
La Marina	16.71	1.75	1.35	0.51
Quemado	17.17	1.25	1.23	0.18
Algodones	9.24	1.11	1.12	0.39

Table 3. Element enrichment factors (EEF) for Mo, V, U and Zn relative to average shale (Wedepohl, 1971). Areas that are relatively enriched are shaded in light grey.

Table 4

Sample #	Location	Formation	Stage	Description	Silicification	Overburden (m)	Temp (˚C)
Z39	MMV, Zipa	Chipaque	Coniacian	Shale, some silt	High	3500-4000	78 (±9), 115 (±17)
LC224	MMV, La Cristalina	Fomeque	Cenomanian	Shale, some silt	Moderate-High	4800	162 (±25)
PE119	EC, Pescana	Chipaque	Campanian	Silty-fine sandstone	High	3500-4000	78 (±9), 115 (±17)
C29	EC, Crucero	Chipaque	Cenomanian	Shale, some silt	Low	3500-4000	78 (±9), 115 (±17)
P145	EC, Pedregal	Fomeque	Barremian	Silty shale	None	7000	208 (±20), 237 (±20)
M364	EC, La Marina	Fomeque	Hauterivian	Shale, some silt	None	7000	208 (±20), 237 (±20)
P1+100	EC, Pedregal	Fomeque	Hauterivian	Shale, silty layers*	None	7000	208 (±20), 237 (±20)
Q1+70	EC, Quemado	Macanal	Valangian	Silty shale	None	8500	249 (±8)
A240	EC, Algodones	Macanal	Valangian	Micaeous siltstone	Low**	8500	249 (±8)

Table 4. Table of data for samples examined during the current study. With data on location, formation, stage, description, degree of silicification, overburden, and temperature. Overburden and temperature data from Mora et al., (2015). Note figures in brackets for temperature refer to the degree of error. Samples arranged in approximate stratigraphic order. MMV = Middle Magdelana Valley, EC = Eastern Cordillera, * with kaolinite and detrital quartz filled burrows, ** irregular wavy authigenic micro-quartz with clay.

Figure 1

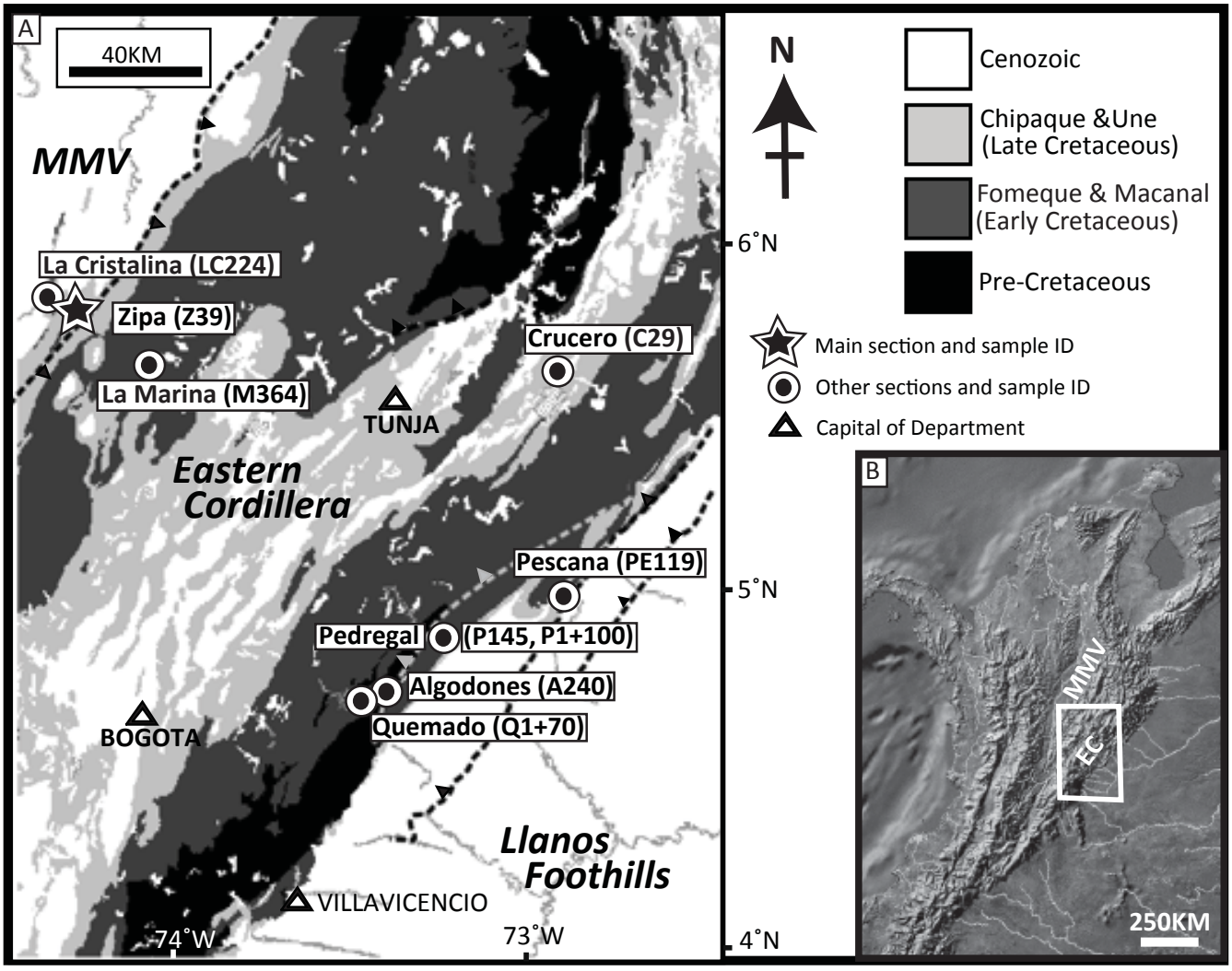
A
40KM
MMV
La Cristalina (LC224)
Zipa (Z39)
La Marina (M364)
Crucero (C29)
TUNJA
Eastern Cordillera
Pescana (PE119)
Pedregal
(P145, P1+100)
Algodones (A240)
Quemado (Q1+70)
BOGOTA
Llanos Foothills
VILLAVICENCIO
74˚W
73˚W
6˚N
5˚N
4˚N
N
Cenozoic
Chipaque &Une (Late Cretaceous)
Fomeque & Macanal (Early Cretaceous)
Pre-Cretaceous
Main section and sample ID
Other sections and sample ID
Capital of Department
B
MMV
EC
250KM

Figure 2

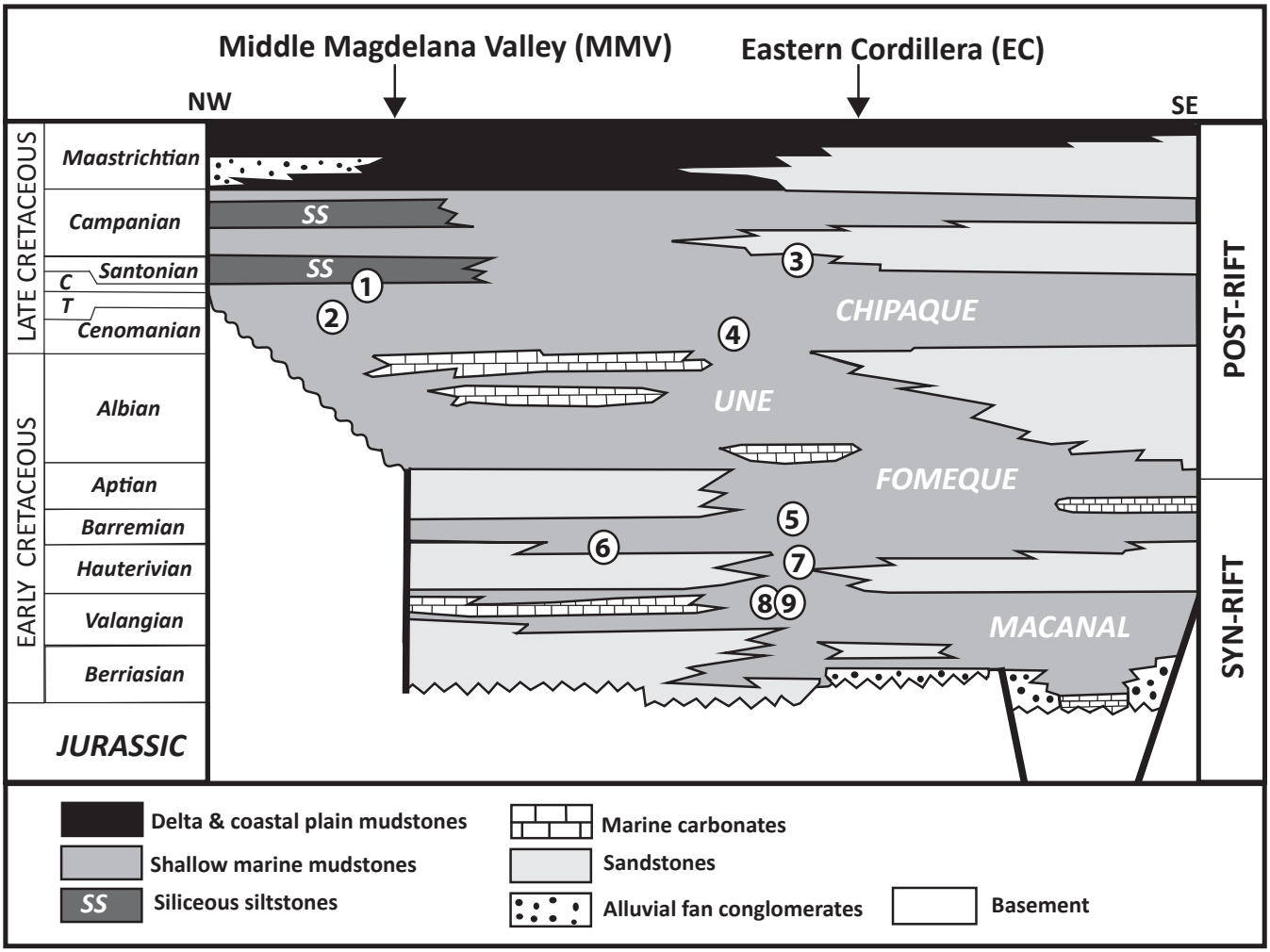
Middle Magdelana Valley (MMV)
Eastern Cordillera (EC)
NW
SE
LATE CRETACEOUS
EARLY CRETACEOUS
Maastrichtian
Campanian
Santonian
C
T
Cenomanian
Albian
Aptian
Barremian
Hauterivian
Valangian
Berriasian
JURASSIC
SS
SS
1
2
3
4
5
6
7
8
9
CHIPAQUE
UNE
FOMEQUE
MACANAL
POST-RIFT
SYN-RIFT
Delta & coastal plain mudstones
Shallow marine mudstones
SS
Siliceous siltstones
Marine carbonates
Sandstones
Alluvial fan conglomerates
Basement

Figure 3

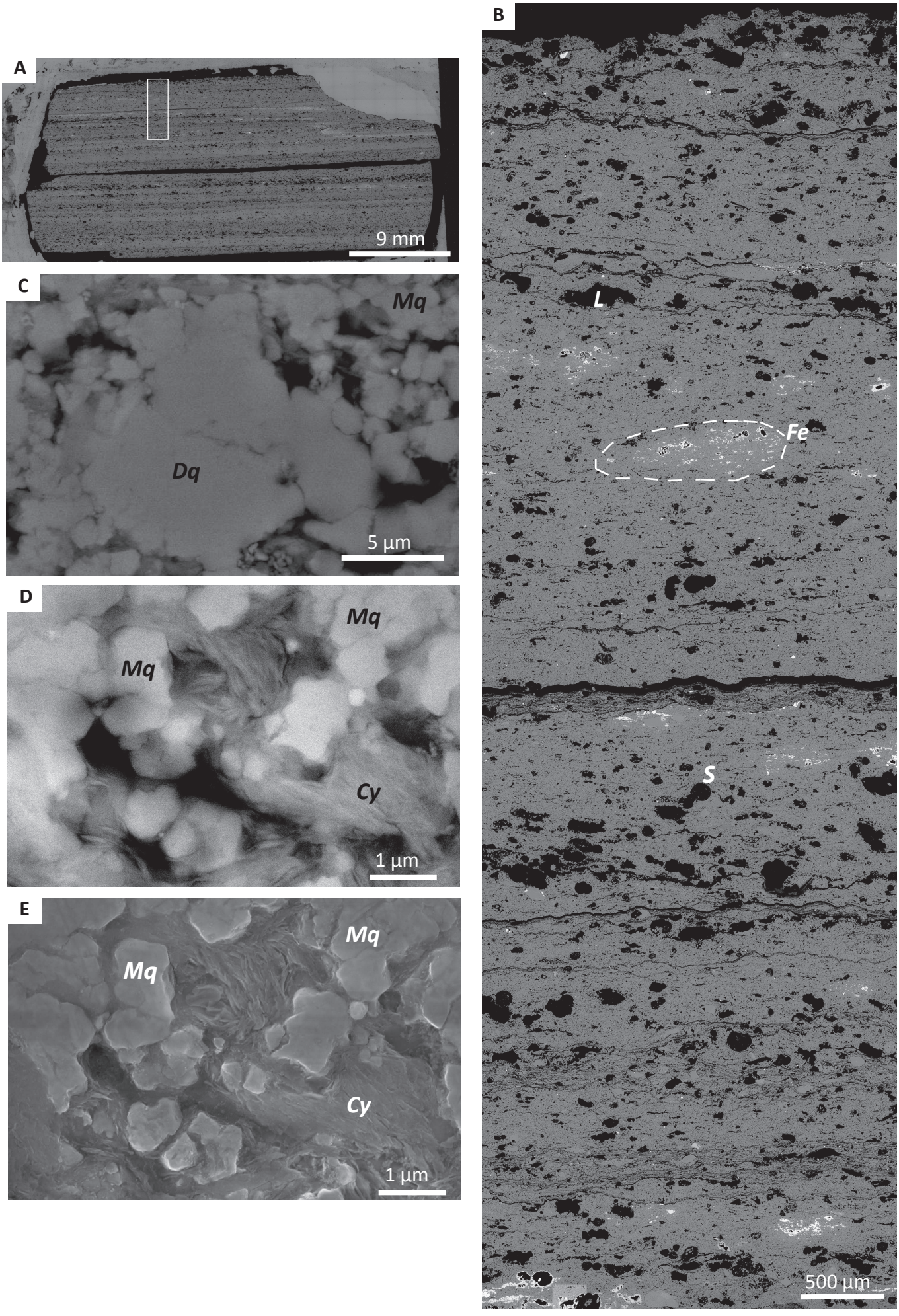

Figure 4

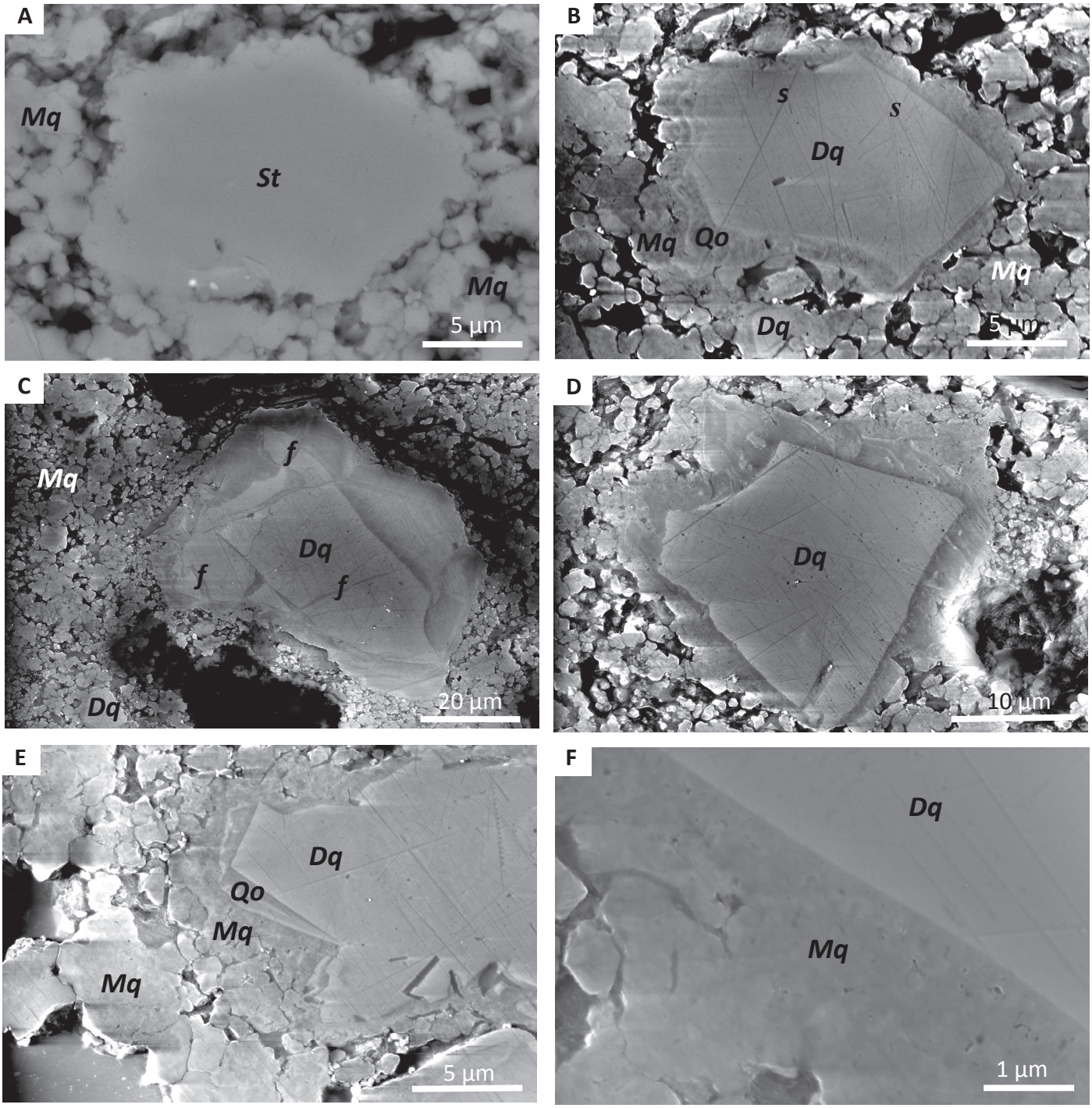
A
Mq
St
Mq
5 µm
B
s
s
Dq
Mq
Qo
Mq
Dq
5 µm
C
f
Mq
Dq
f
f
Dq
20 µm
D
Dq
10 µm
E
Dq
Qo
Mq
Mq
5 µm
F
Dq
Mq
1 µm

Figure 5

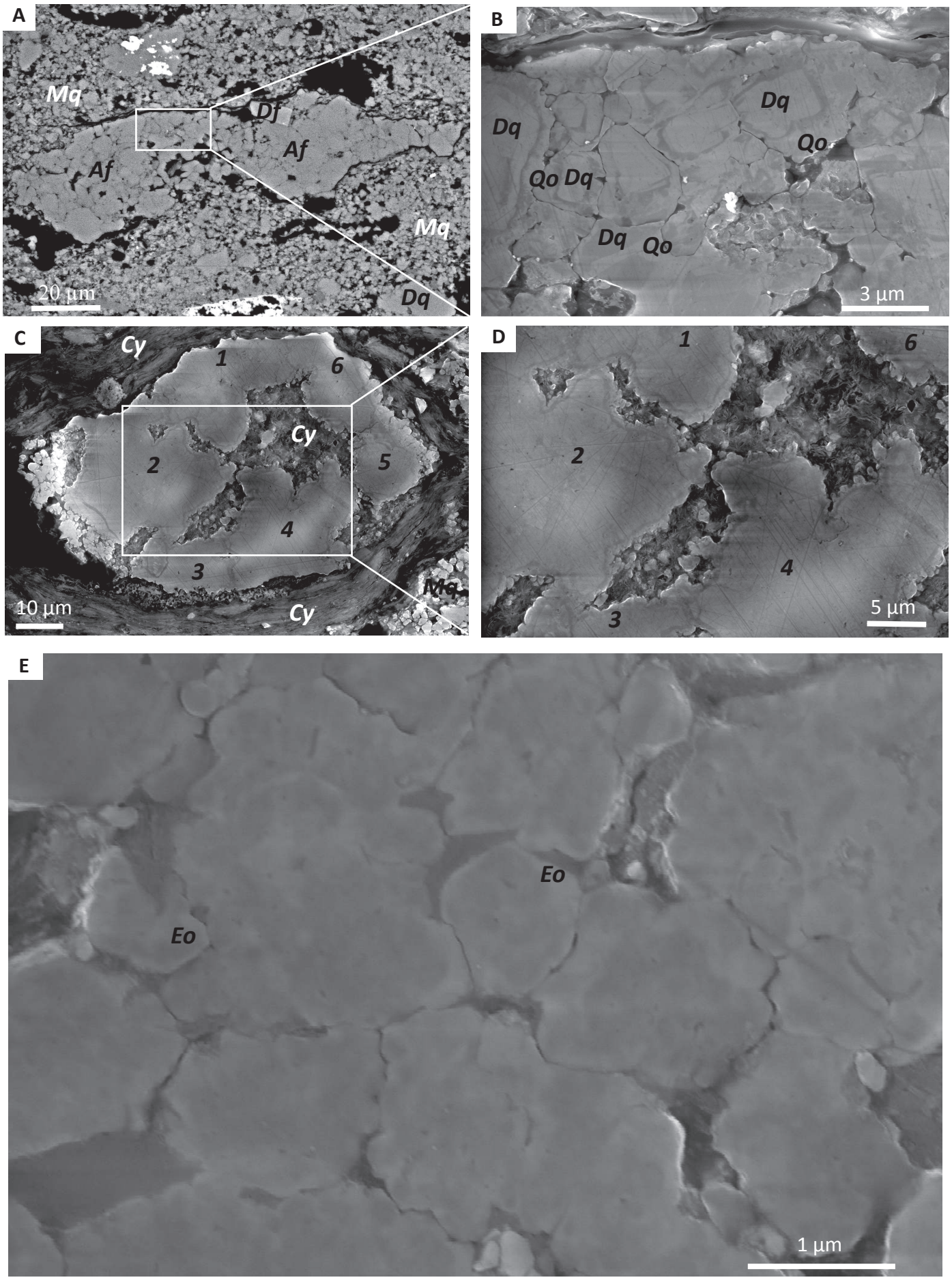
A
Mq
Df
Af
Af
Mq
20 µm
Dq
B
Dq
Dq
Qo
Qo Dq
Dq
Qo
3 µm
C
Cy
1
6
Cy
2
5
4
3
Mq
10 µm
Cy
D
1
6
2
4
3
5 µm
E
Eo
Eo
1 µm

Figure 6

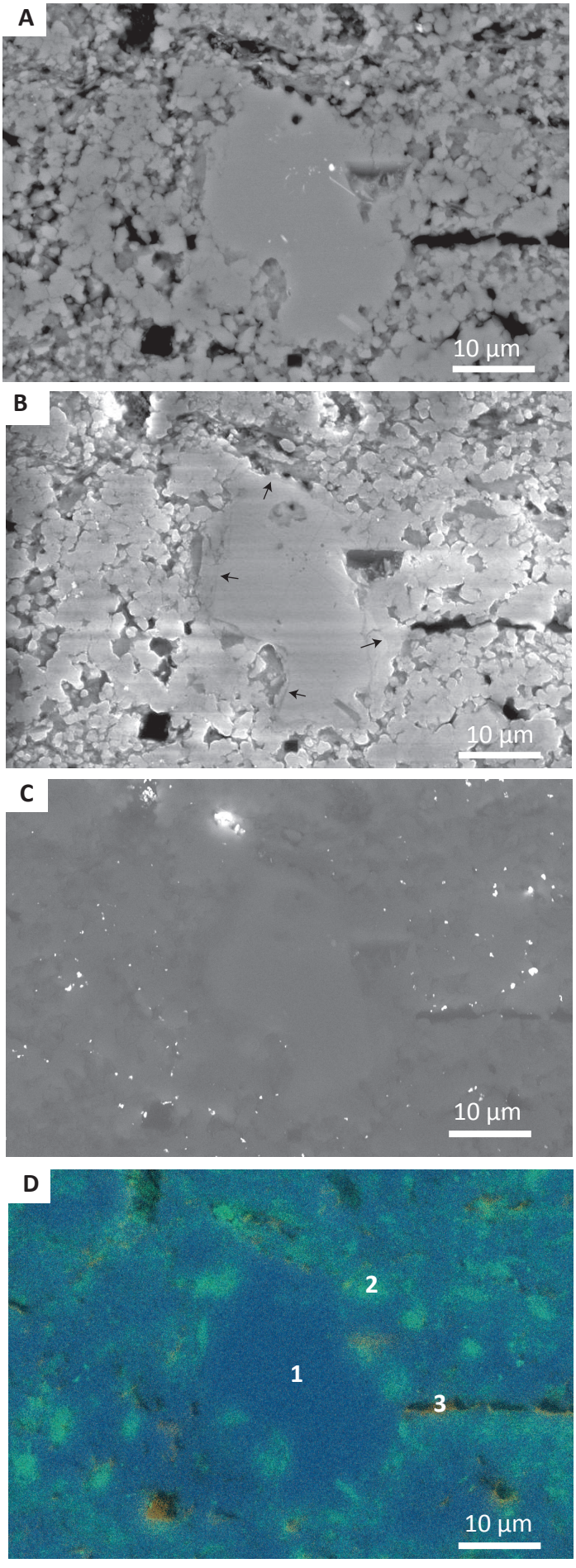

Figure 7

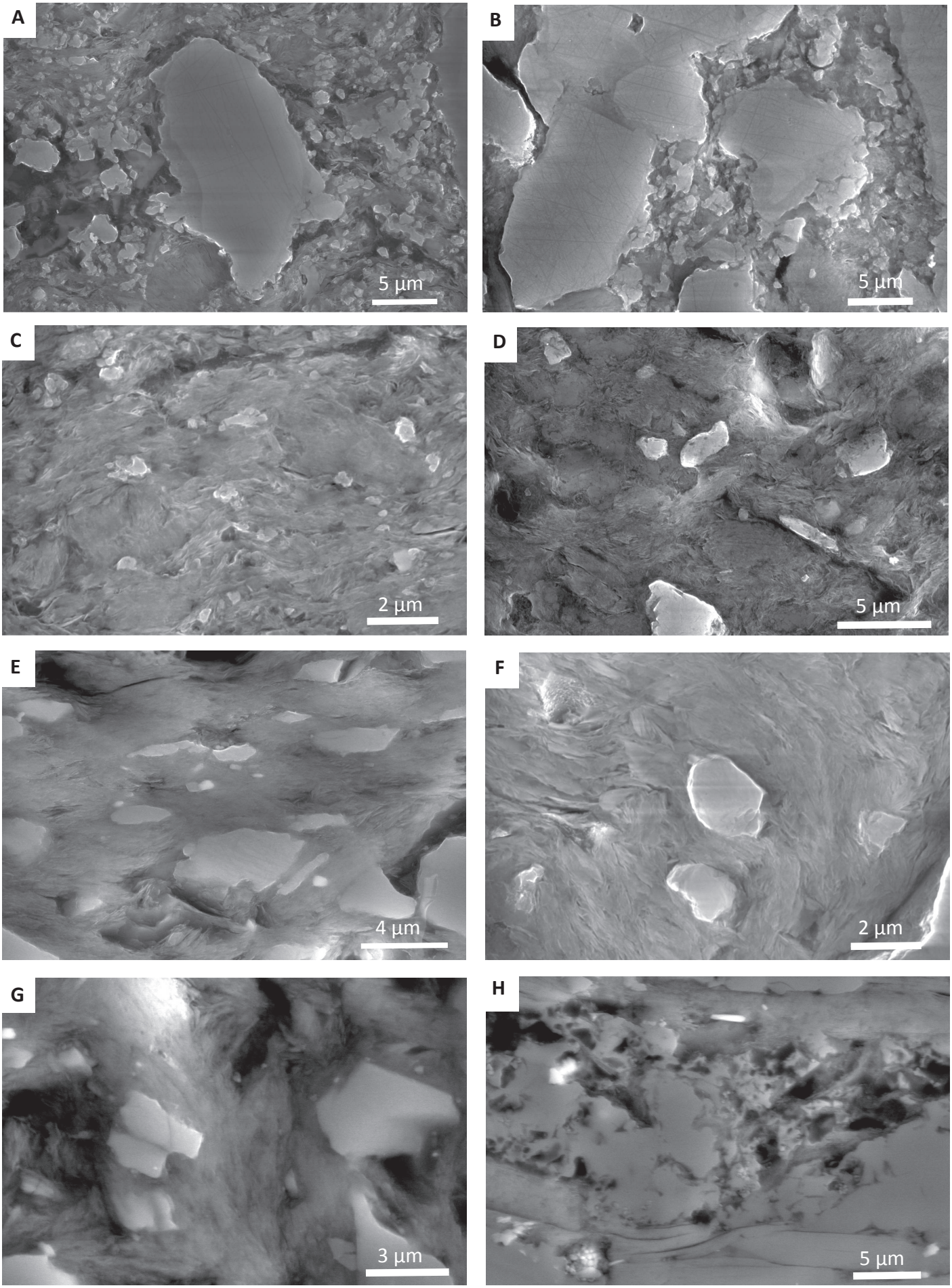

Figure 8

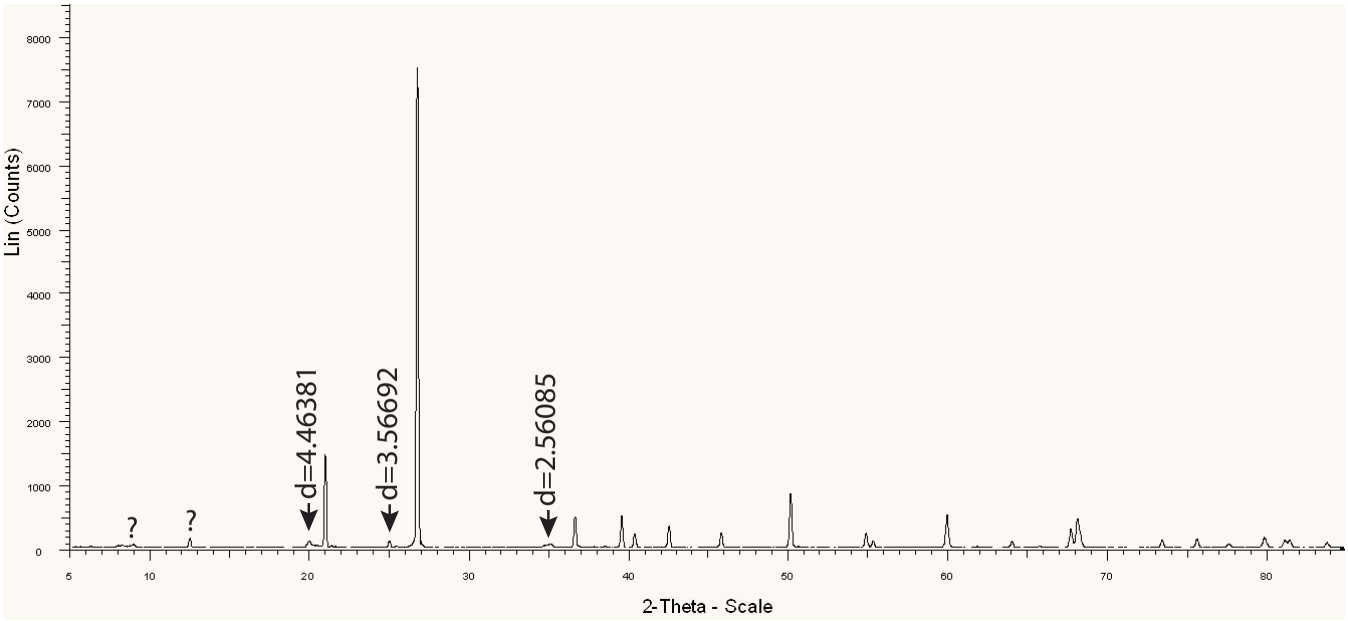
Lin (Counts)
8000
7000
6000
5000
4000
3000
2000
1000
0
?
?
d=4.46381
d=3.56692
d=2.56085
5
10
20
30
40
50
60
70
80
2-Theta - Scale

Figure 9

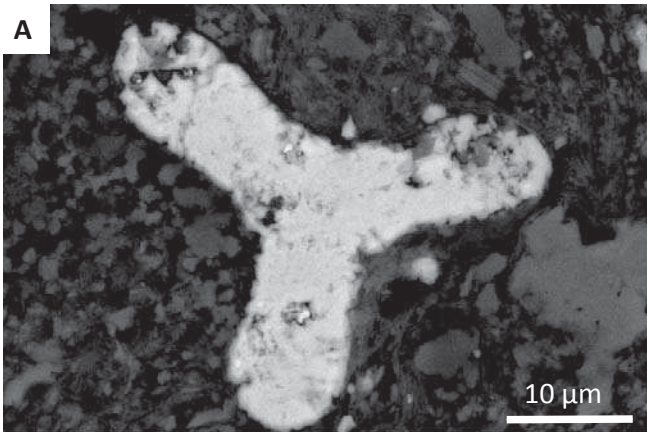

Figure 10

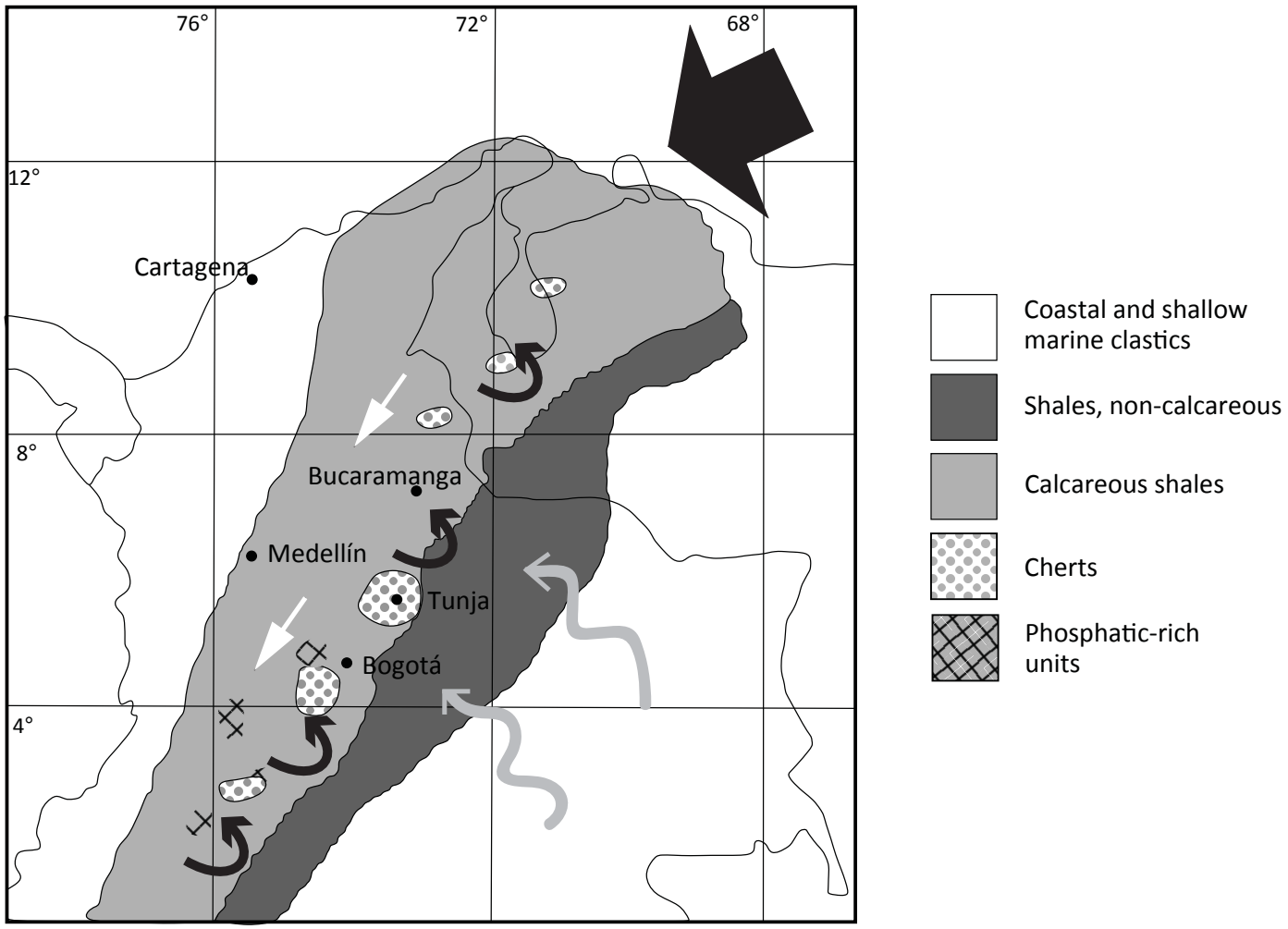
76°
72°
68°
12°
8°
4°
Cartagena
Bucaramanga
Medellín
Tunja
Bogotá
Coastal and shallow marine clastics
Shales, non-calcareous
Calcareous shales
Cherts
Phosphatic-rich units